A Multiparameter Integration Method and Characterization Study of Chipless RFID Sensors With Spiral Shape

Guochun Wan, *Member, IEEE*, Zicheng Jiang, and Liyu Xie

***Abstract*— In the field of structural health monitoring (SHM), with the development of chipless radio frequency identification (RFID) technology, various single-parameter sensors have gradually moved toward integration, such as strain and encoding, temperature and humidity, and other multiparameter sensors. However, due to the fixed structure of these multiparameter sensors, their states cannot be flexibly controlled, and it is difficult to distinguish and locate them when multiple sensors exist simultaneously. In this article, a novel chipless RFID sensor for multiparameter sensing is designed. The sensor integrates encoding, humidity, and strain measurements without using a traditional chip-based design. A broadband antenna is designed to match the operating frequency band of the sensor. This integration of multiple parameters is made possible by the sensor's unique design and the use of a compatible antenna, which enables the measurement of different physical parameters simultaneously. Furthermore, flexible combinations of the three parameters are achieved through wired or wireless reconfiguration methods, which allow for the sensor's states to be reconfigured during measurement. As a result, this sensor can achieve multiple states, making it more versatile and efficient in monitoring various parameters. In the future, this approach could be combined with selfpowering devices and more advanced wireless modules to achieve long-term state control of sensors in large-scale infrastructure structures, providing a new method for modern building health monitoring applications, from integrated sensor control to sensor differentiation and localization.**

***Index Terms*— Chipless radio frequency identification (RFID), humidity detection, multiparameter, reconfiguration control, strain detection, structural health monitoring (SHM).**

I. INTRODUCTION

DUE to the uncertainty of working environments, modern large-scale building facilities often experience cyclic loading and chemical corrosion, leading to deterioration phenomena, such as strain, corrosion, and cracking in building materials. Over time, these issues can result in safety accidents, causing significant economic and property losses as well as injuries to personnel. In this context, structural health monitoring (SHM) of large-scale building structures becomes especially crucial in ensuring the safety and stability of these structures. In the field of SHM, the traditional method of inspection is through nondestructive testing (NDT) to periodically examine the structure of facilities, such as visual, ultrasonic, and electromagnetic (EM) testing and assessment techniques [1], [2]. However, most of these techniques are active wired systems. Considering the volume and complexity of large structures, the deployment, maintenance, and debugging of these systems are very cumbersome. At the same time, the supporting monitoring equipment is expensive, the probing time is long, and the data transmission distance is short. These disadvantages have limited the development of this technology. However, with the development of technology, the emergence of chipless radio frequency (RF) identification technology has given SHM new vitality and plays an important role in the field of SHM. Most of the current research on SHM is still limited to stress characteristics [11], [12], and the monitoring of physical parameters in the environment where the structure is located, such as temperature and humidity, gas content, pH, and other parameters, has not yet been fully investigated. Meanwhile, the difficulty of changing the state after fabrication is an inherent drawback of traditional chipless radio frequency identification (RFID) sensors. Therefore, there is a need to explore the field in relation to these drawbacks.

RFID system includes two types of tags: chip and chipless. Compared with chip RFID, chipless RFID is more widely studied due to its lower cost. This technology uses radio waves to identify remote chipless tags and extract encoded, strain, and other information stored in the tag's trapped circuit structure from the backscattered waves.

For RFID strain sensors, initially, chip-based rectangular patch antennas (RPAs) were used as strain sensors, which could be used to simultaneously detect the stress and gaps on the surface of the test piece [3]. Subsequently, Cho et al. [4] made improvements by adding a configuration network of Schottky diodes to the upper radiation surface to remove the chip's limitation and reduce the mutual interference between signals. For chipless strain sensing, there are various approaches. Mita and Takahira [5], [6], [7] used mechanically constructed sensors, which detect strain by the elastic bending of an extended plastic material, but they only can store peak strain values. Thompson et al. [8] later used resonant

Manuscript received 22 May 2023; revised 23 July 2023; accepted 4 August 2023. Date of publication 21 August 2023; date of current version 1 September 2023. This work was supported in part by the General Program of National Natural Science Foundation of China, "Research on the principles of passive sensing and structural deformation monitoring methods based on antennas without stress patch" under Project 52078375 and in part by the Top Discipline Plan of Shanghai Universities-Class I. The Associate Editor coordinating the review process was Dr. George Dan Mois. *(Corresponding author: Guochun Wan.)*

Guochun Wan and Zicheng Jiang are with the Department of Electronic Science and Technology, Tongji University, Shanghai 200092, China (e-mail: wanguochun@tongji.edu.cn; jiang_zi_cheng@163.com).

Liyu Xie is with the Department of Disaster Mitigation for Structures, Tongji University, Shanghai 200092, China (e-mail: liyuxie@tongji.edu.cn).

Digital Object Identifier 10.1109/TIM.2023.3306820

characteristics and a resonant cavity wireless strain sensor to measure strain by displacement, where the displacement of the rod under stress causes a change in cavity volume, and thus a change in resonant frequency. He et al. [9] integrated strain sensors into clothing based on electronic textile materials, which could be used to measure stress and achieve body movement-based control by converting measurement signals into inputs for digital devices. Cheng et al. [10] proposed an RFID sensor tag for real-time monitoring of metal surface strain magnitude and direction based on a C-type resonator array, which can monitor strain amplitude and direction with higher sensitivity and simpler structure.

However, the traditional focus in the field of SHM is still on the variation of mechanical properties [11], [12], and the monitoring of physical parameters in the environment where the structure is located, such as temperature and humidity, gas content, pH, and other parameters, has not yet been adequately investigated. With the gradual expansion of the application scenarios of RFID technology in various aspects of society, the demand for RFID sensors for multiple environmental parameters is expanding, and therefore, there is a need to develop chipless RFID sensors for multiparameter sensing. Amin et al. [13] designed a multiparameter RFID sensor without a chip, which integrates coding, humidity, and temperature threshold measurement by combining a helical resonator with temperature-sensitive material phenanthrene and humidity-sensitive material polyvinyl alcohol, which provides a good idea of the methodology for monitoring temperature and humidity.

Despite the advantages of chipless RFID technology in SHM, it is still under intensive research. With the gradual development of building structures, more and more sensors are required to be used in the field of SHM, and the size and encoding capability of chipless RFID tags is one of the main challenges nowadays, which has led many scholars to make exploratory attempts on the introduction of encoding capability of chipless RFID tags. Vena et al. [14] proposed a compact-sized chipless RFID tag consisting of 20 C-shaped resonators. This C-type structure was later combined with phase shift and frequency position coding and applied to hybrid coding technology [15]. Islam et al. proposed two novels compact chipless RFID systems. The chipless tags in the DP and OI systems consist of horizontally and vertically polarized "I" slot resonators of different lengths, with sufficient frequency-encoded data capacity, data density, and direction-insensitivity. Chen et al. [16] improved the coding capacity and integrated strain parameters by enhancing the U-shaped resonator in the same physical area.

Currently, wireless systems are moving toward intelligence for fast, secure, and reliable communication. In the field of SHM, the level of intelligence that can be introduced into multifunctional wireless systems is severely limited by the fact that the parameters of conventional chipless RFID tags related are fixed and cannot be reconfigured once they have been fabricated. Therefore, many scholars have made relevant attempts to control the intelligent aspects of RFID tags, and reconfigurable antennas provide enough flexibility and adaptability to the rapidly changing needs of wireless systems and their operating environments. Michel et al. [17] proposed a reconfigurable chipless RFID tag with enhanced antenna performance by using two modules, namely, a spiral traveling wave antenna and an array of four resonant slot antennas. The desired configuration can be selected by RF switches according to specific scenarios. Tajin and Dandekar [18] proposed a low-cost, easy-to-manufacture, and pattern reconfigurable ultra high frequency (UHF) RFID reader antenna that can radiate four electronically switchable beams in the azimuth plane. This not only increases the coverage area of traditional RFID applications but also opens the door for implementing human RFID sensors and indoor positioning applications. In the field of SHM, the chipless RFID-based sensor localization system has been suffering from the problem of inaccurate information transmission [19], and it is important to distinguish the identity information of sensors. If the reconfigurable feature can be more widely applied to the SHM field, and the controllable feature of sensors can be utilized to change the ID code of sensors in real time to obtain the information, which will greatly improve the accuracy of distinguishing and locating the sensors in a large number of sensors.

In summary, the traditional chipless RFID sensors in the field of SHM have the disadvantages of detecting a single parameter and being unable to be reconfigured. The current research on multiparameter chipless RFID sensors for simultaneous detection of structural strain, humidity, and characterization codes in the SHM field is not enough, and there is no effective intelligent control and wireless transmission strategy for the reconfigurable function of multiparameter sensors. Therefore, in this article, a multiparameter chipless RFID sensor is designed by combining new organic materials and RF switches to integrate coding, humidity, and strain functions, and PIN diodes are used to realize reconfigurable characteristics. A retransmission matched cross-polarized transceiver antenna is also used for wireless detection [20], eliminating the need for bulky horn antennas. In addition, a wireless dynamic control scheme for multiparameter sensors and matching is proposed based on the wireless control module, which provides a new way of thinking for multiphysical field control of structural body sensors with multiscenario data extraction.

A. Contribution of This Article

This article addresses the directions of multiparameter integration and reconfiguration characteristics of chipless RFID sensors, and the main contributions are as follows.

1) Based on the foundation required for the study, for the coding part, the conversion theory of the prototype low-pass filter to the spiral bandstop filter is derived.
2) Simulation fusion of coding, humidity, and strain parameters on chipless RFID was carried out, and the three functions of the designed sensor are independent of each other and can be flexibly combined. A transceiver broadband antenna for this multiparameter sensor was also designed for the implementation of wireless detection.
3) The physical sensor was fabricated and humidity and strain monitoring experiments were conducted to verify its functionality.

4) A low-cost wireless reconfigurable control method is proposed with a PIN diode as the core, combined with a wireless communication module, to realize the wired/wireless function switching and coding reconfiguration of the multiparameter sensor.

B. Full-Article Arrangement

Section I describes the development status of chipless RFID sensors and the background and research situation at home and abroad. Section II introduces some theoretical foundations and derivations involved in the design of chipless RFID sensors and completes the integration of sensors and their parameter design optimization. Section III verifies the functionality of the designed sensors through experiments and conducts relevant analysis and discussion. Meanwhile, a low-cost wired/wireless reconfiguration method with a PIN diode as the core is proposed, and the consistency is checked by experimental and simulation data. Sections IV and V discuss and summarize the experiments.

II. DESIGN OF RFID SENSOR BASED ON SPIRAL BANDSTOP FILTER

Microstrip patch antennas typically consist of a conductive patch, a dielectric substrate, and a ground plane. The antenna performance can be adjusted by changing the shape and size of the conductive patch. Compared to conventional sensors, microstrip patch antennas have the advantages of simple structure, lightweight, low production cost, easy integration, and adjustable operating frequency. Therefore, they have been widely used in many fields.

This section proposes a chipless RFID multiparameter sensor based on a microstrip spiral bandstop filter with four different parts: a rectangular strain cell for strain monitoring through the strain occurring in the patch resulting in a shift of the resonant frequency; three stable spiral microstrip resonator circuits for encoding that form the ID part of the tag; a spiral microstrip resonator circuit structure with a polyimide (PI) film attached for humidity monitoring; and finally a reconfigurable control part with a PIN diode incorporated to achieve controllable and observable functionality.

A. Filter Coding Principle

The input impedance and output impedance of the coding unit in the bandpass filter circuit are not constant and will change with the variation of the coding bits. In addition, the input and output impedance of the encoding units in the bandpass filter circuit are not constant and will change with the number of encoding bits. Moreover, the reflections between bandpass filter circuit units will affect the bandpass characteristics, resulting in a further increase of mismatch loss in the passband of the unit. Therefore, this article adopts the bandstop filter for the related design.

Fig. 1 shows the equivalent circuit of an n-bit encoding structure. According to the microstrip theory, a quarter-wavelength open-ended microstrip line at ω_0 can be considered as an RLC resonant circuit, and the circuit element sizes are given by the following equations:

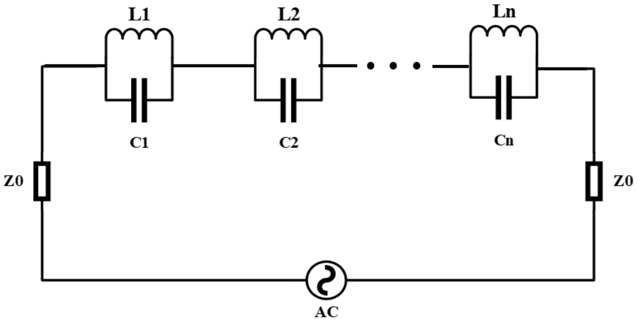

Fig. 1. Equivalent circuit.

$$R = Z_{0i}\alpha l_i \tag{1}$$

$$L = \frac{\pi Z_{0i}}{4w_i} \tag{2}$$

$$C = \frac{4}{\pi Z_{0i} w_i} \tag{3}$$

$$Z_{0o} = \frac{4Z_0}{g_i \Delta\pi} \tag{4}$$

where Z_{0o} is the characteristic impedance of the microstrip short cut line, l_{0o} is the length of the microstrip line, φ is the attenuation coefficient, and g_i is taken as the coefficient of the first-order low-pass filter.

Combined with the relationship between the characteristic impedance of the microstrip line and the characteristic impedance of the transmission line in the literature [21], the final bandstop filter coding unit circuit model can be obtained as shown in (5)–(8). With the RLC circuit quantization model, the expected operating frequency and bandwidth of the RFID sensor can be designed, followed by further optimization of the design of the encoding unit shape:

$$R = Z_{0i}\alpha l_i \tag{5}$$

$$L = \frac{Z_{0i}}{8f} \tag{6}$$

$$C = \frac{2}{Z_{0i}\pi^2 f} \tag{7}$$

$$Z_{0i} = \frac{2Z_{0o}}{\Delta W \pi}. \tag{8}$$

B. Integrated Sensor Design

According to the derived theoretical model, the final multiparameter integrated sensor schematic is shown in Fig. 2 by combining the rectangular strain cell and the spiralized bandstop filter. The final model parameters were selected by optimization through several simulations and are listed in Table I.

Fig. 3 shows the resonant response curve of S_{21} obtained by optimizing the multiparameter sensor design in the RF simulation software HFSS, which generates five resonant frequencies, 0.95, 1.608, 1.86, 2.24, and 2.8 GHz, respectively. The coupling effect between different units is greatly reduced.

Fig. 4 shows the current distribution at the resonant frequency points corresponding to each part. At the operating

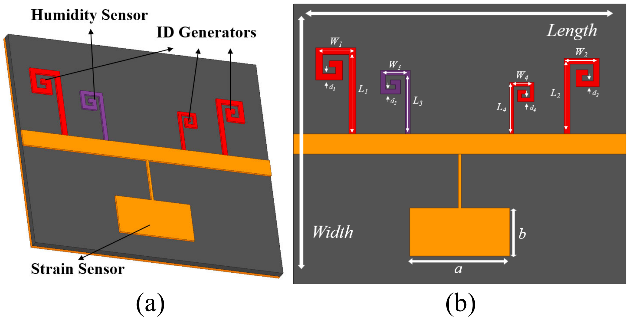

Fig. 2. Geometry of the proposed sensor. (a) 3-D model. (b) Front view.

TABLE I
OPTIMIZED INTEGRATED SENSOR PARAMETER RESULTS

Value(mm)							
Length	60	L_1	16.000	W_1	7.20	d_1	1.200
Width	52	L_2	14.048	W_2	6.322	d_2	1.054
a	18	L_3	11.840	W_3	5.328	d_3	0.888
b	9	L_4	9.600	W_4	4.320	d_4	0.72

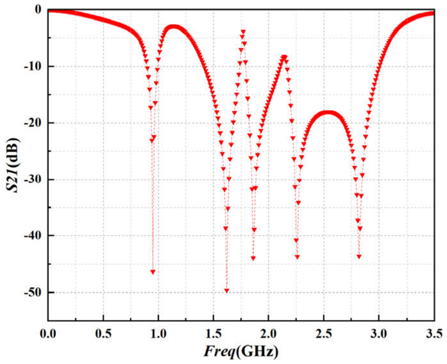

Fig. 3. S_{21} results of integrated sensor in HFSS simulation.

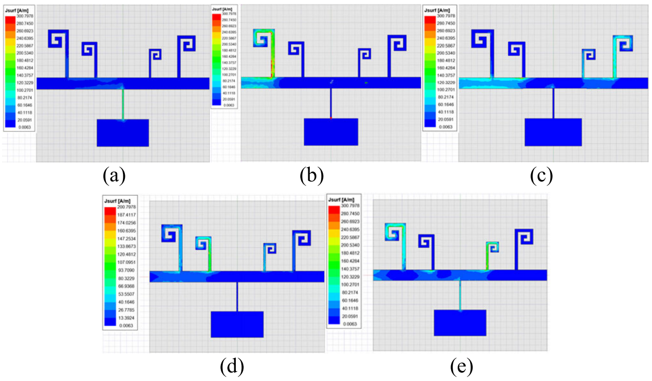

Fig. 4. Simulation results of current distribution at the resonant frequency of each part of the integrated sensor. (a) 0.95 GHz. (b) 1.608 GHz. (c) 1.86 GHz. (d) 2.24 GHz. (e) 2.8 GHz.

frequency of each part, the currents in other parts are very weak, so the coupling effect of each part of the structure is weak, and the functions of each part of the sensor are clearly divided and the parameters are reasonably optimized.

C. Simulation of Strain Section Sensing

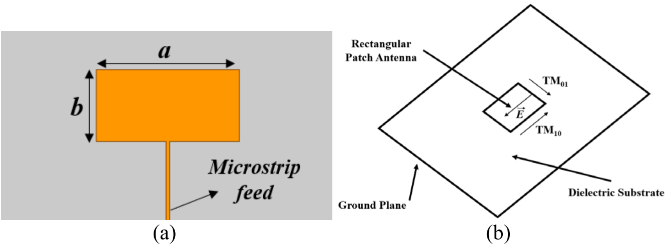

Fig. 5. (a) Rectangular patch transmission line model diagram. (b) Working mode schematic.

The rectangular microstrip patch antenna sensor is used for the strain sensing part in this section, and based on the transmission line model, the normalized antenna resonant frequency shift is derived and simulated to be linearly proportional to the strain, which provides a theoretical basis for subsequent experimental verification. The transmission line model diagram and circuit model of the rectangular patch are given in Fig. 5.

RPA is made of a dielectric substrate sandwiched between two conductive layers, namely a radiation patch and ground plane. RPA has two basic resonant modes: TM_{10} mode with current flowing along the patch length L direction and TM_{01} mode with current flowing along the patch width W direction. The resonant frequency f_{10} in the rectangular microstrip patch length L, width W, and TM_{10} mode can be calculated by deriving the following equation:

$$L=\frac{1}{4f_r\sqrt{u_0\varepsilon_0}}\sqrt{\frac{2}{\varepsilon_r+1}}=\frac{c}{2f_r}\sqrt{\frac{2}{\varepsilon_r+1}} \tag{9}$$

$$W=\frac{1}{2f_r\sqrt{\varepsilon_e}}-2\Delta L \tag{10}$$

$$\Delta L=0.412h\left(\frac{\varepsilon_e+0.3}{\varepsilon_e-0.258}\right)\left(1+\frac{10h}{L}\right)^{-\frac{1}{2}} \tag{11}$$

$$f_{10}=\frac{c}{2(L+2\Delta L)\sqrt{\varepsilon_e}} \tag{12}$$

where c represents the speed of light in a vacuum, ε_e represents the effective dielectric constant of the substrate, and ΔL is the edge extension length of the radiation field.

If the height of the substrate is much smaller than the radiating patch size (i.e., $h \ll W$ and $h \ll L$), the effective dielectric constant can be approximated as the dielectric constant of the substrate. In addition, the line extension ΔL can be neglected. In this case, the (12) can be simplified as follows:

$$f_{10}=\frac{c}{2L\sqrt{\varepsilon_e}}. \tag{13}$$

The offset δf_{10} of the antenna frequency can be expressed according to the variation of the patch length L and the substrate dielectric constant ε_r as follows:

$$\delta f_{10}=\frac{\partial f_{10}}{\partial \varepsilon_r}\delta\varepsilon_r+\frac{\partial f_{10}}{\partial L}\delta L. \tag{14}$$

The general form of the normalized frequency shift δf_{10} in the final TM_{10} model is as follows:

$$\frac{\delta f_{10}}{f_{10}}=-K_{\mathrm{TL}}\delta T-K_{\varepsilon L}\varepsilon_L. \tag{15}$$

Similarly, it can be deduced that the general form of the normalized frequency shift δf_{01} in TM_{01} mode is shown in

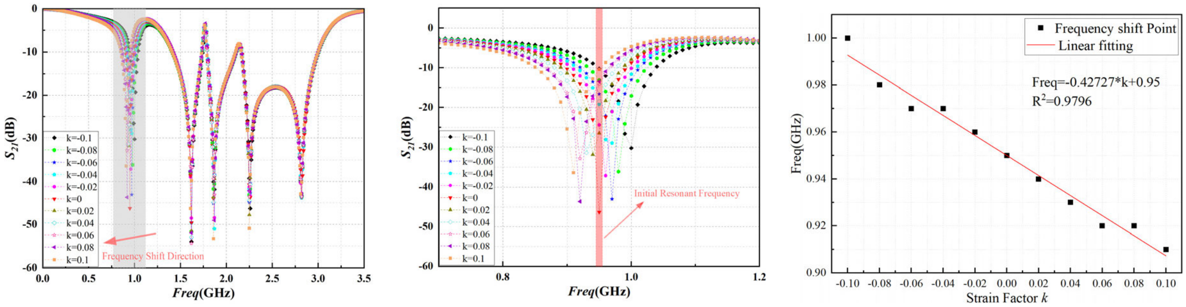

(a) (b) (c)

Fig. 6. (a) S_{21} results of integrated sensor after strain. (b) S_{21} results of strain frequency shift in the enlarging part. (c) Linear fitting line of strain frequency shift.

the following equation:

$$\frac{\delta f_{01}}{f_{01}} = -K_{\mathrm{TW}}\delta T - K_{\varepsilon W}\varepsilon_L \tag{16}$$

where $K_{\varepsilon L}$ and $K_{\varepsilon W}$ denote the strain sensitivity along the length and width of the patch, respectively, while K_{TL} and K_{TL} denote the temperature sensitivity along the length and width of the patch, respectively. Different feed position modes are different, and the sensor designed in this article is TM_{01} mode, so the *b*-direction in Fig. 5 is dominant for strain.

It can be seen from (16) that the normalized antenna resonant frequency shift of the rectangular patch part is linearly proportional to the strain when the temperature is constant, and the coefficient is negative due to the Poisson effect.

Based on the above theoretical derivation, simulation experiments were conducted in the simulation software HFSS. The strain stretching is simulated by setting the strain factor k as the variation parameter for the designed integrated sensor for sweeping the reference. The overall simulation results in the *b*-direction are shown in Fig. 6, which shows that the strain unit resonance frequency is monotonically decreasing, while the other units are insensitive, in accordance with the theoretical derivation.

Fig. 6(b) shows the local frequency shift of the rectangular patch. The data are linearly fit to obtain $\mathrm{Freq} = -0.42727k + 0.95$, $R^2 = 0.9796$, and the fit line intercept is 0.95 GHz, which is basically equal to the initial resonant frequency, and the sensitivity is -0.42727 kHz/$\mu\varepsilon$ by converting the units to microstrain.

D. Humidity Unit Sensing Analysis

PI refers to a class of polymers containing an imide ring (-CO-NR-CO-) on the main chain, which is one of the organic polymer materials with the best overall performance. As a special engineering material, it is commonly used as a dielectric material in electronic devices, and its dielectric constant is an important physical parameter, which has been widely used in aviation, aerospace, microelectronics, nano, liquid crystal, separation film, laser, and other fields.

The study said that the dielectric constant of the PI film has a certain relationship with the humidity of the surrounding environment. When the ambient humidity is low, the number of adsorbed water molecules in the PI film is small and the dielectric constant is more stable. However, when the ambient humidity increases, more water molecules are adsorbed on the surface of the PI film, and these water molecules form an electric dipole-like structure in the PI film, which leads to a change in the dielectric constant of the PI film. The exact extent of this relationship depends on factors, such as the structure and properties of the PI film itself, as well as the specific value of the ambient humidity. However, in general, as the ambient humidity increases and the water absorption gradually increases, the general trend of the dielectric constant of PI films increases gradually due to the high dielectric constant of water ($\varepsilon \approx 80$) [22], and this increasing trend is generally nonlinear.

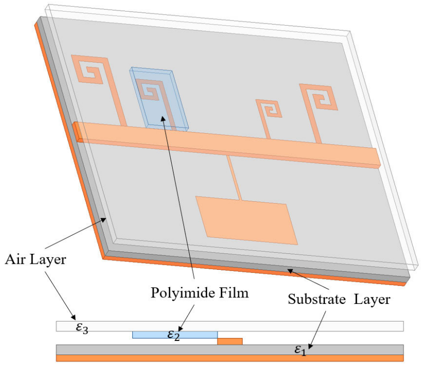

Fig. 7. Sensor model covered with coating.

The coverage coating model is shown in Fig. 7, and the resonant frequency f of the equivalent patch antenna is shown in the following equation:

$$f = \frac{cn}{2L\sqrt{\varepsilon_e'}} \tag{17}$$

where c is the speed of light; n is the resonant frequency order, here taken as 1; and ε' is derived from the three dielectric constants [23]. The increase in the equivalent dielectric constant after covering the film will make the frequency smaller.

Therefore, the theoretical derivation of the PI film to monitor air humidity results in a constant decrease of the corresponding resonant frequency as the humidity increases.

E. Reconfiguration Characterization Simulation

The integrated sensor is designed with a 4-bit coding part to identify different sensors by their coding, for example, "1011" and "1110" are two different integrated sensors. According to the traditional method, the sensor is produced, its code ID is

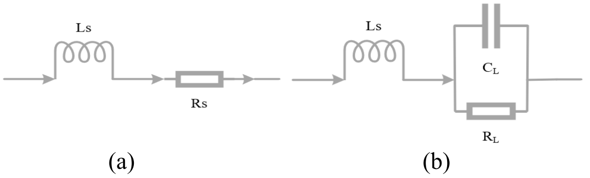

Fig. 8. PIN diode RF switch two-state equivalent circuit diagram. (a) ON state. (b) OFF state.

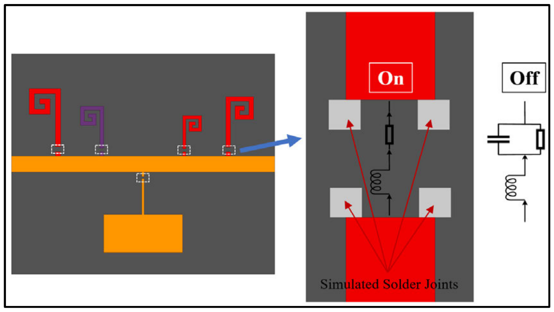

Fig. 9. Modeling two states of PIN diode RF switch in HFSS Software.

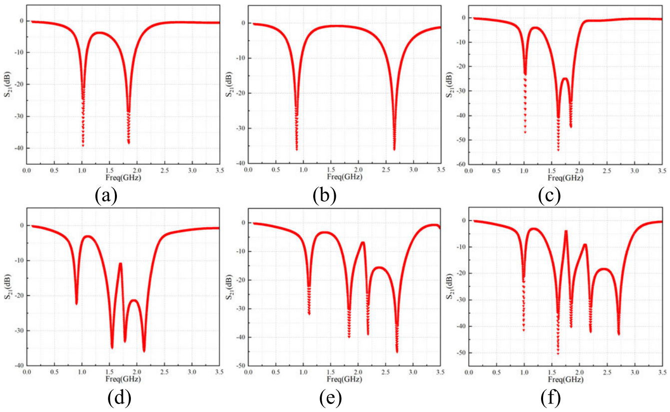

Fig. 10. Reconfigurable simulation results for six different states. (a) “10100.” (b) “10001.” (c) “11100.” (d) “11110.” (e) “10111.” (f) “11111.”

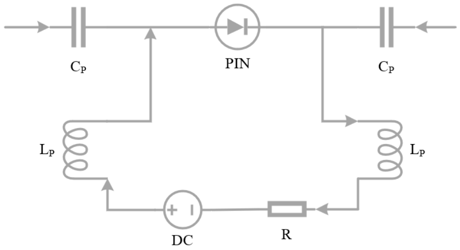

Fig. 11. Bias circuit schematic.

fixed, cannot be changed. For chip RFID sensors, it is possible to read and write multiple times to change the content carried. Therefore, it is more flexible in terms of the range of use and the amount of information carried. In order to allow the coding unit and different functional units printed on the substrate to change and switch flexibly. Enabling RF switch on the sensor to achieve code reconfigurability and function reconfigurability will be discussed below.

To facilitate integration, the PIN diode RF switch is used. The equivalent circuit of the PIN diode RF switch in both ON and OFF states is given in Fig. 8.

It can be seen that the PIN diode RF switch, in the case of conduction, can be equated to a circuit with an inductor in series with a small resistor; while in the cutoff state, it can be equated to a circuit with an inductor and capacitor connected in parallel with a resistor, and the resistance value is relatively large at this time. According to the above model, the model is established in the simulation software for parameter discussion, and the model schematic is shown in Fig. 9.

The Lumped RLC function available in HFSS provides a flexible modular modeling capability, where multiple interconnected structures can be used for the elements that need to be combined. It is worth noting that the device needs to be soldered to the sensor, so several parts are set up to simulate the effect of solder joints. In the simulation process, through circuit optimization design, the selected PIN diode OFF state equivalent resistance is 5000 Ω, equivalent capacitance is 0.5 pF, equivalent inductance is 0.6 nH; ON state equivalent resistance is 0.1 Ω, equivalent inductance is 0.6 nH. In order to ensure the consistency of subsequent experiments as much as possible, the parameters of the diode selected in the simulation process should be consistent with the actual experimental situation.

By changing the simulation parameters, six states of “10100,” “10001,” “11100,” “11110,” “10111,” and “11111” were simulated, and the simulation results are shown in Fig. 10. It can be seen that the reconfiguration of each part is basically realized by PIN diode, and the reconfigurable characteristics of the sensor, whether it is a coding unit or a functional unit, can be realized.

As with diodes in general, the different operating states of the PIN diode need to be controlled with the help of a bias circuit. Because of the application scenario in high-frequency circuits, it is necessary to add some external collector components as isolation parts between the bias circuit and the ac/dc in order to make the RF switch work properly, as shown in Fig. 11. The Cp is the capacitor, mainly to prevent the interference and damage of the dc part of the bias voltage to the RF part. Lp is the inductor part, which is generally placed near the ac circuit, in order to prevent the RF part from disturbing the signal of the ac part. The resistor R is to limit the current and prevent the bias circuit from directly connecting to the power supply and breaking the diode. By adjusting the magnitude and direction of the bias voltage dc to control the ON state of the PIN diode, thus controlling the access to the RF path.

F. Broadband Transceiver Antenna Design

For the design of high-capacity chipless RFID tags, ultra-wideband technology has been proposed and widely used, which not only enables the development of robust chipless RFID systems, but also has promising features, such as low cost, compactness, and lightness. However, for the common rectangular or circular patch antenna as a wireless RFID tag transceiver antenna, there are shortcomings, such as lower antenna gain and shorter infinite output distance. Therefore, based on the integrated sensor designed in the previous section, a new broadband chipless RFID antenna scheme is proposed to realize wireless transmission. In the experiments, the antennas

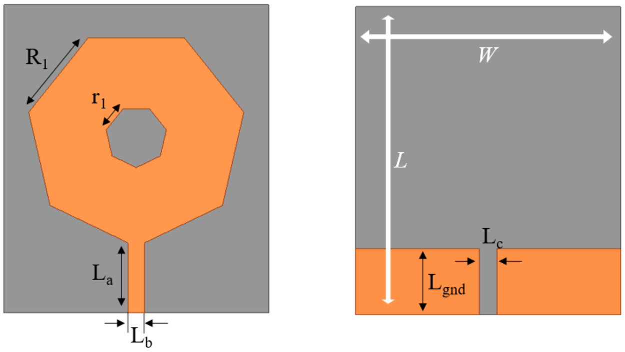

(a) (b)

Fig. 12. Broadband antenna diagram. (a) Broadband antenna front side. (b) Broadband antenna back side.

TABLE II

BROADBAND ANTENNA SIZE PARAMETERS

Parameter	L	W	R_1	r_1
Value(mm)	70	60	21.69	6.074
Parameter	L_a	L_b	L_c	L_{gnd}
Value(mm)	15.90	3.72	4.0	15.0

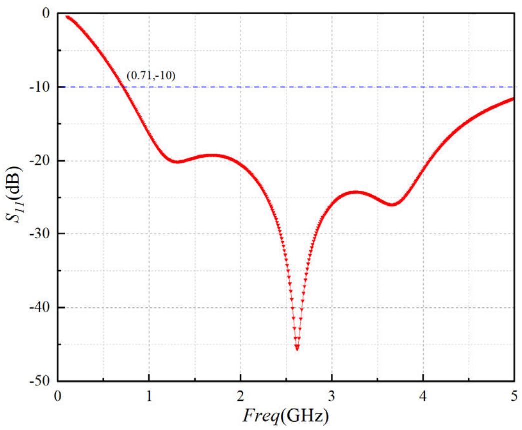

Fig. 13. S_{11} simulation parameter of broadband antenna.

are placed in cross-polarization direction, aiming to minimize the crosstalk between the interrogation and response signals.

The broadband antenna is based on the basic heptagon, and on this basis, relevant iterative optimization is carried out to obtain a better transceiver effect in the operating band range, and the final design structure is shown in Fig. 12, and the final antenna parameter dimensions are shown in Table II.

The results of the simulated S_{11} parameters are shown in Fig. 13, the S_{11} parameters of the antenna are below -10 dB in the frequency band from 0.71 to 5 GHz. This result is in accordance with the requirements of the operating band (0.95–2.8 GHz), the depth of the antenna waveform is large in this operating band, which indicates that it has good transceiver performance and can meet the measurement requirements of multiparameter integrated sensors. The antenna has good transceiver performance and can meet the measurement requirements of multiparameter integrated sensors.

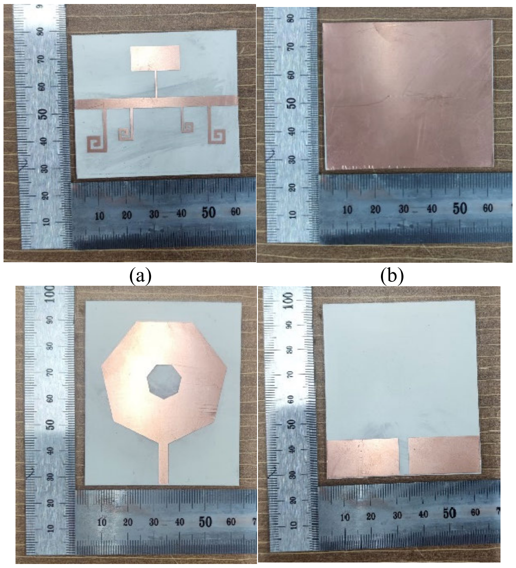

(a) (b) (c) (d)

Fig. 14. Physical view of integrated sensor and broadband antenna. (a) Integrated sensor front side. (b) Integrated sensor back side. (c) Broadband antenna front side. (d) Broadband antenna back side.

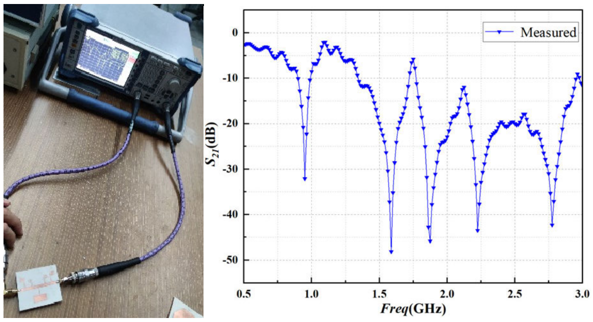

(a) (b)

Fig. 15. (a) Wired measurement scenario. (b) S_{21} parameter for wired measurement.

III. EXPERIMENTAL VERIFICATION OF INTEGRATED SENSORS

A. Wireless/Wired Measurement Comparison

All the physical objects fabricated in this section are made of Rogers RT 3003 HF laminate material with a thickness of 1.51 mm and a copper foil thickness of 17.5 μm above and below. Fig. 14 shows the physical diagram of the fabricated integrated sensor and broadband antenna.

Using a microwave network analyzer (ZVL, Network Analyze, 9 kHz–3 GHz) for testing, the wired test scenario and test results are shown in Fig. 15. It can be seen that the five trapped waves are 0.95, 1.608, 1.86, 2.24, and 2.88 GHz. Compared to the simulation results, they are basically the same.

For the wireless measurements, the purchased log-periodic dipole antenna combined with the broadband antenna of its own design was used in the microwave darkroom for the experiments, and the cross-polarization method was used to place the measurements in order to minimize the crosstalk between the interrogation and response signals. The measurement results are shown in Fig. 16. Considering the effects of environmental noise and process, it can be seen that although there is more clutter, the overall measured S_{21} parameters can

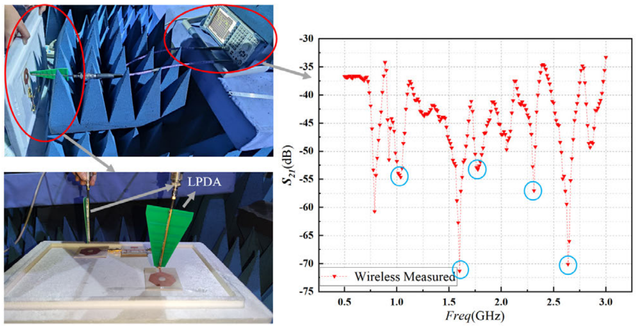

(a) (b)

Fig. 16. (a) Wireless measurement scenario. (b) S_{21} parameter for wireless measurement.

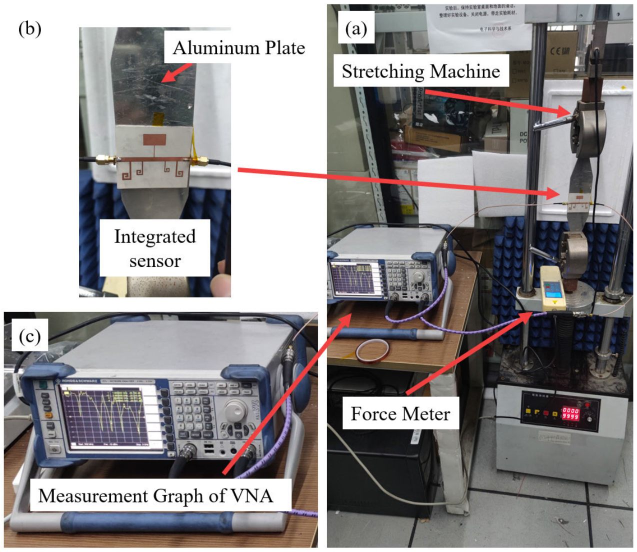

Fig. 17. (a) Strain measurement scenario. (b) Integrated sensor. (c) Measurement graph of VNA.

be seen to be basically in accordance with the simulation results.

B. Strain Experimental Design

To construct an integrated sensor strain detection system to test the strain performance of RFID-integrated sensors. The whole testing platform includes the designed RFID sensor, vector network analyzer (VNA, ZVL, Network Analyze, 9 kHz–3 GHz), tensile machine (SJV-30000, Siwei Instrument Company Ltd., China), and aluminum plate to be tested, as shown in Fig. 17.

The strain experiments were carried out by stretching, which was performed using the SJV-30000 stretching machine. According to the Saint-Venant's principle, in order to ensure that the strain sensing unit of the tag is adsorbed on the aluminum plate at both ends with uniform force, the aluminum plate to be tested should be as long as possible. Therefore, a rectangular specimen with dimensions of 250 × 50 × 1.5 mm was used, and its two ends were fixed on the chuck of the tensile machine, and the tension was applied to the aluminum plate by changing the position of the chucks at both ends of the tensile machine, and the tension value was displayed in real time by a force meter.

Since the strain transfer of the tensile machine has a certain hysteresis, the tensile behavior does not stay at the expected value accurately. In order to improve the accuracy of the experiment, five measurements were performed at the same tension indication and averaged to eliminate the effect of strain transfer hysteresis. In which the stress of the stretching machine could not be precisely controlled as an integer, so the step sizes were not equal. The results of fitting the tensile data in the width direction (b-direction in Fig. 5) are shown in Fig. 18. From the measured data, it can be seen that there is an obvious linear relationship between the resonant frequency of the sensor strain cell and the strain variable, which is consistent with the results of the theoretical derivation and simulation experiments conducted earlier.

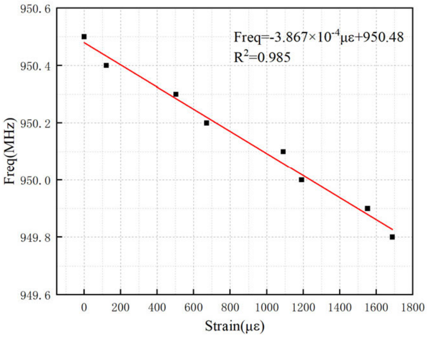

Fig. 18. Fitting results of the actual strain parameter.

C. Humidity Experimental Design

The selection of moisture-sensitive materials as substrates can reflect the changes of relative humidity in the environment to some extent; however, few pressure-resistant materials are currently available in the field of SHM that also have good sensitivity to changes in relative humidity. In this experiment, the aim is to explore a multiparameter sensor design that is easy to integrate and has good humidity sensitivity performance.

Through the previous analysis in the humidity theory section, this experiment uses PI film for humidity sensing, which is glued to the designed humidity unit through adhesive and simulates the change of relative humidity in the environment by humidifying it in a foam box, as shown in Fig. 19 for the specific experimental scenario. A white foam-sealed container was used to construct an airtight humidity space with holes drilled at both ends for the hygrometer (Sigma AR847+) probe and humidifier power cord to pass through, and the tape was used to fill the holes during the experiment to ensure a sealed environment. The humidity inside the container was then changed by the humidifier, and the results of S_{21} parameters were measured under different humidity levels after the hygrometer showed stable numbers. Among them, desiccant is used to slow down the humidity change and ensure the full absorption of moisture by the PI film to avoid the humidity change too fast to affect the experimental data.

The measured S_{21} results are shown in Fig. 20, including the overall S_{21} results and the local resonant frequency change process of the humidity unit. Considering that the specific humidity values in the experiment could not be precisely controlled, the data points were collected in a discrete and small number. Several interpolation methods were tried, and

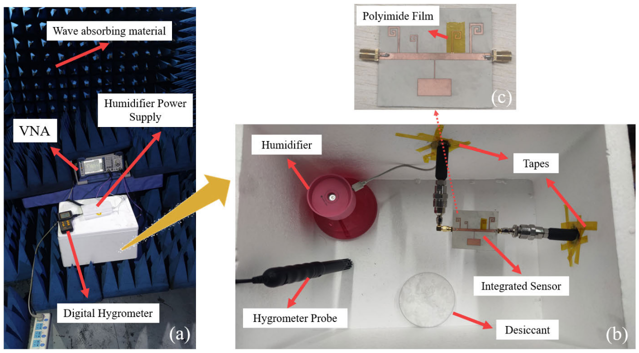

Fig. 19. (a) Humidity monitoring experimental scenario. (b) Foam box internal scene. (c) Integrated sensor with PI film.

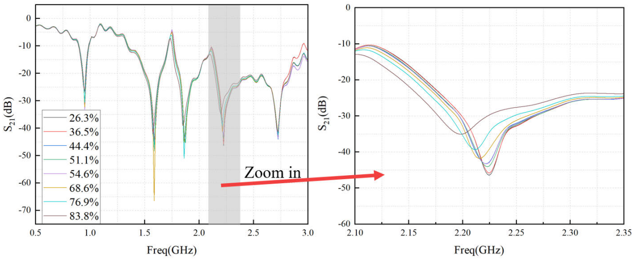

(a) (b)

Fig. 20. (a) S_{21} parameter measured under different humidity. (b) S_{21} parameter curve of the enlarged section.

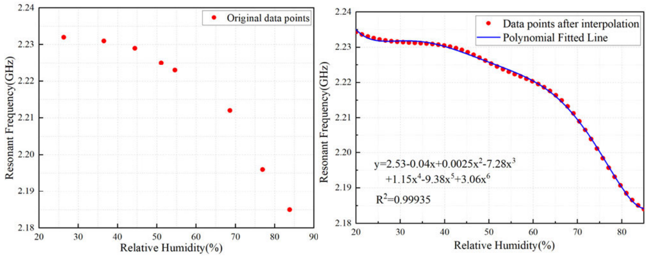

(a) (b)

Fig. 21. (a) Resonant frequency points measured at different humidity levels. (b) Curve plot fit after interpolation using the Akima method.

finally, Akima interpolation was used for data expansion. The results are more in line with the actual trend, as shown in Fig. 21. When the relative humidity is low, the change in resonant frequency is small, and as the relative humidity rises, the change in resonant frequency becomes larger and larger, which is consistent with the theory and proves that it is feasible to use the change in the degree of frequency shift with relative humidity to transmit the realization of humidity monitoring in practical applications.

At the end of the experiment, the closed container was opened, and the sensor was left for a period of time to recover its original state after waiting for the water vapor to escape. During this process, the humidity gradually decreases as the water vapor evaporates, and the resonant frequency of the coding unit covered with the PI membrane moves to the lower right due to the decrease in humidity, proving that the sensor can be reused.

D. Reconfiguration Experimental Design

The principles of reconfiguration characteristics were introduced in the previous section and verified by relevant simulations. In this section, the aim is to explore a method that enables flexible control of the above-integrated sensors, capable of code changes and function switching.

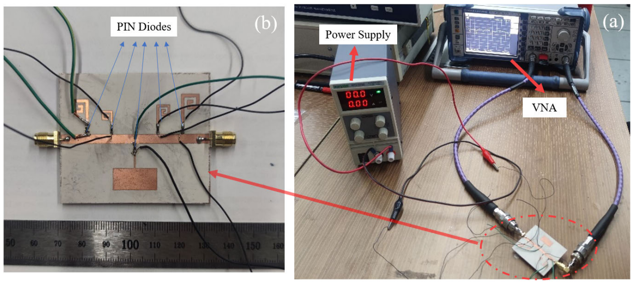

Fig. 22. (a) Reconfigurable experimental scenario. (b) Integrated sensor with PIN diodes.

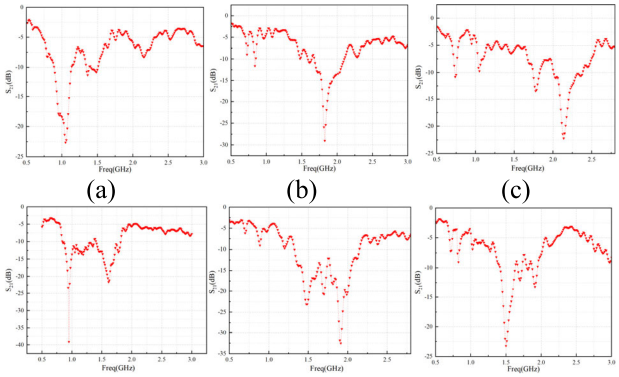

(a) (b) (c)

(d) (e) (f)

Fig. 23. S_{21} parameters measured in six different states. (a) "10000." (b) "00100." (c) "00010." (d) "11000." (e) "01100." (f) "01000."

To ensure consistency between simulation and experiment, a PIN diode of type BAR64-02V was chosen to be used, which corresponds to the parameters set by the previous simulation. The power supply model used in the experiments is the Wanptek KPS 1505D, which is connected to the PIN diodes through wires. The overall measurement scenario and the sensor with integrated PIN diodes are shown in Fig. 22. The power supply outputs 0 V when the PIN diodes are OFF, and 2 V when they are ON. On the sensor with five integrated PIN diodes for "10000," "00100," "00010," "11000," "01100," and "01000" six states were measured physically, S_{21} parameters are shown in Fig. 23.

As can be seen in Fig. 23, with −20 dB as the dividing line, the results are fully consistent with its transmission characteristics, and the error is basically negligible considering that the previously described bias circuit has not been added to reduce interference. The test results show that the S_{21} amplitude value of the designed multiparameter sensor is more consistent with the simulation results, and the band resistance characteristics in each region can be effectively identified. $2^5 = 32$ sensor states can be effectively reconfigured by five independent groups of PIN diodes, and code reconfiguration and function reconfiguration can be effectively realized.

In addition, in order to better switch different states through PIN diodes, it is proposed to combine the wireless module and removable power supply to propose a wirelessly controlled state-switching method, whose overall framework is shown in Fig. 24. The PC sends commands to the wireless transmission module to control the switching of power at both ends of different PIN diodes, so as to achieve the effect of switching

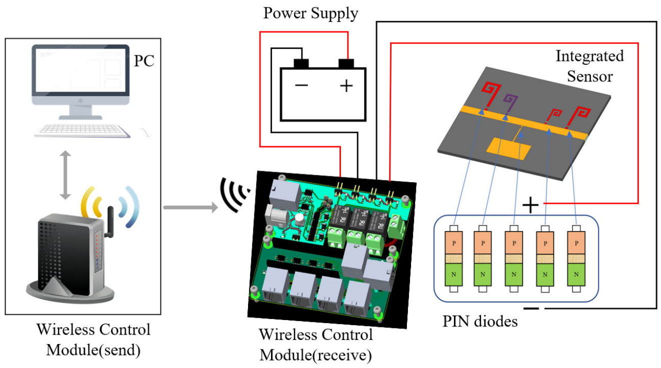

Fig. 24. Block diagram of the state switching method controlled by the wireless module.

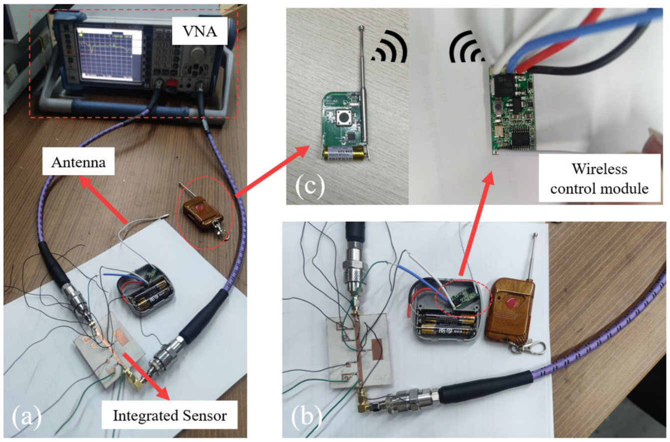

Fig. 25. (a) Wireless state switching experimental scenario. (b) Enlarged view of the experimental scenario. (c) Wireless control module.

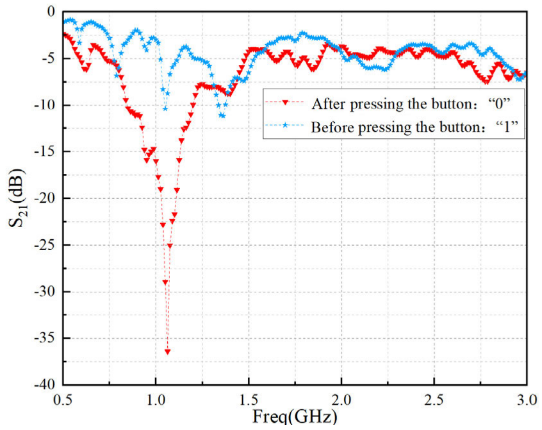

Fig. 26. S_{21} parameters measured before and after switch control.

different states. The actual experiments in this article use an RF module instead of a PC to wirelessly control the ON–OFF of the power supply at both ends of the PIN diode, mainly for the verification of the function.

The specific scenario built in the laboratory is shown in Fig. 25. Here, the PIN diodes of the strain unit are connected to the wireless control module, where the transmitter module is assembled with a remote-control housing, and its interior is shown in Fig. 25(c). The power supply is powered by two 1.5 V batteries. When the red button is pressed in the transmitter module, the voltage on both sides of the PIN diode is turned on, and the state of the strain cell is switched from "0" to "1," and the measurement results before and after the switching of the S_{21} parameter are shown in Fig. 26. It can be seen that the wireless module basically achieves the function of wirelessly switching the state of the integrated sensor, and after several experiments, it can be effectively controlled within 20 m, which basically realizes the long-distance control of the sensor state switching.

IV. DISCUSSION

Traditional single-parameter chipless RFID sensor technology has its advantages in measurement accuracy. However, it suffers from limitations such as a single type of measured parameter and a lack of reconfigurability. Therefore, the integration of multiple parameters and reconfigurable control holds practical value and greater flexibility in the field of SHM.

In this study, by combining novel organic materials and RF switches, we have successfully integrated encoding, humidity, and strain functionalities, leading to the design of a chipless RFID sensor capable of simultaneously monitoring strain parameters in building structures while obtaining encoding and humidity data. The implementation of PIN diodes enables reconfigurability, allowing us to switch sensor functionalities and reconstruct encoding by controlling the power supply of the PIN diode. This contributes to providing more accurate sensor information and offers a feasible approach for realizing multiparameter detection and reconfigurable capabilities in the SHM field.

The introduction of multiple parameters inevitably affects the precision of the sensor. For humidity monitoring, ensuring stable data requires a high standard in the fabrication process of polymer coatings. Moreover, the integration of multiple parameters unavoidably increases the size of the sensor and manufacturing costs. However, compared to large-scale building structures, the sensor size proposed in this study remains applicable. Concerning the encoding part, the current integration is limited to 3 bits, resulting in limited capacity. In summary, future optimization efforts can be directed toward refining the fabrication process, miniaturizing the sensor, and enhancing encoding capacity.

V. CONCLUSION

In this article, a multiparameter chipless RFID sensor applied in the field of SHM is designed to realize the integration of three functions of the chipless RFID sensor: coding, humidity, and strain. At the same time, a broadband transceiver antenna matching the operating frequency band is designed for it. The three functions of the designed sensor are independent of each other and can be flexibly combined by means of an RF switch. The experiment proves that the coding part has stability; the strain part of the rectangular patch resonant frequency change and the degree of strain have a linear relationship; the humidity part is in line with the theoretical derivation and simulation results, and as the temperature and humidity increase, the resonant frequency decreases faster, which can play the role of high temperature and high humidity early warning. The overall realization of the mechanical parameters and environmental parameters in the structure of the simultaneous monitoring, and also comes with the coding function.

In addition, flexible switching of different states is achieved by integrating PIN diodes, which solves the shortcomings of traditional chipless RFID sensors with only one state. Meanwhile, a low-cost wireless control method is proposed in combination with a wireless control module and removable power supply, which provides a new idea for a more flexible implementation of sensor state control.

In the future, this approach can be used in combination with selfpowered devices and better wireless modules to achieve long-term state control of sensors, while the flexible and controllable characteristics of sensors can be used to better locate sensors and obtain data in environments with a large number of sensors, and to make more accurate predictions of structural body safety and multidirectional losses in multiphysical fields.

REFERENCES

[1] F. Hernandez-Valle, A. R. Clough, and R. S. Edwards, "Stress corrosion cracking detection using non-contact ultrasonic techniques," *Corrosion Sci.*, vol. 78, pp. 335–342, Jan. 2014, doi: 10.1016/j.corsci.2013.10.018.

[2] G. Y. Tian, Y. He, I. Adewale, and A. Simm, "Research on spectral response of pulsed eddy current and NDE applications," *Sens. Actuators A, Phys.*, vol. 189, pp. 313–320, Jan. 2013, doi: 10.1016/j.sna.2012.10.011.

[3] X. Yi, C. Cho, J. Cooper, Y. Wang, M. M. Tentzeris, and R. T. Leon, "Passive wireless antenna sensor for strain and crack sensing—Electromagnetic modeling, simulation, and testing," *Smart Mater. Struct.*, vol. 22, no. 8, Aug. 2013, Art. no. 085009, doi: 10.1088/0964-1726/22/8/085009.

[4] C. Cho, X. Yi, D. Li, Y. Wang, and M. M. Tentzeris, "Passive wireless frequency doubling antenna sensor for strain and crack sensing," *IEEE Sensors J.*, vol. 16, no. 14, pp. 5725–5733, Jul. 2016, doi: 10.1109/JSEN.2016.2567221.

[5] A. Mita and S. Takahira, "Health monitoring of smart structures using damage index sensors," *Proc. SPIE*, vol. 4696, pp. 92–99, Jun. 2002.

[6] A. Mita and S. Takhira, "A smart sensor using a mechanical memory for structural health monitoring of a damage-controlled building," *Smart Mater. Struct.*, vol. 12, no. 2, pp. 204–209, Apr. 2003, doi: 10.1088/0964-1726/12/2/307.

[7] A. Mita and S. Takahira, "Damage index sensor for smart structures," *Struct. Eng. Mech.*, vol. 17, nos. 3–4, pp. 331–346, Mar. 2004.

[8] D. J. Thomson, D. Card, and G. E. Bridges, "RF cavity passive wireless sensors with time-domain gating-based interrogation for SHM of civil structures," *IEEE Sensors J.*, vol. 9, no. 11, pp. 1430–1438, Nov. 2009, doi: 10.1109/JSEN.2009.2027407.

[9] H. He, X. Chen, L. Ukkonen, and J. Virkki, "Clothing-integrated passive RFID strain sensor platform for body movement-based controlling," in *Proc. IEEE Int. Conf. RFID Technol. Appl. (RFID-TA)*, Sep. 2019, pp. 236–239.

[10] X. Cheng, Y. Yu, F. Wang, and G. Tian, "A novel multiresonant chipless RFID tag for directional strain measurement on metal surface," *IEEE Trans. Microw. Theory Techn.*, vol. 71, no. 2, pp. 916–925, Feb. 2023, doi: 10.1109/TMTT.2022.3213655.

[11] G. C. Wan, M. M. Li, Y. L. Yang, L. Xie, and L. Chen, "Patch-antenna-based structural strain measurement using optimized energy detection algorithm applied on USRP," *IEEE Internet Things J.*, vol. 8, no. 9, pp. 7476–7484, May 2021, doi: 10.1109/JIOT.2020.3039277.

[12] G. Wan, M. Li, M. Zhang, L. Kang, and L. Xie, "A novel information fusion method of RFID strain sensor based on microstrip notch circuit," *IEEE Trans. Instrum. Meas.*, vol. 71, pp. 1–10, 2022, doi: 10.1109/TIM.2022.3161718.

[13] E. M. Amin, N. C. Karmakar, and B. W. Jensen, "Fully printable chipless RFID multi-parameter sensor," *Sens. Actuators A, Phys.*, vol. 248, pp. 223–232, Sep. 2016, doi: 10.1016/j.sna.2016.06.014.

[14] A. Vena, E. Perret, and S. Tedjini, "A fully printable chipless RFID tag with detuning correction technique," *IEEE Microw. Wireless Compon. Lett.*, vol. 22, no. 4, pp. 209–211, Apr. 2012, doi: 10.1109/LMWC.2012.2188785.

[15] A. Vena, E. Perret, and S. Tedjini, "Chipless RFID tag using hybrid coding technique," *IEEE Trans. Microw. Theory Techn.*, vol. 59, no. 12, pp. 3356–3364, Dec. 2011, doi: 10.1109/TMTT.2011.2171001.

[16] L. Chen, L. Liu, L. Kang, Z. Wan, G. Wan, and L. Xie, "A multibranch U-shaped tunable encoding chipless RFID strain sensor for IoT sensing system," *IEEE Internet Things J.*, vol. 10, no. 6, pp. 5304–5320, Mar. 2023, doi: 10.1109/JIOT.2022.3221938.

[17] A. Michel, M. Rodriguez Pino, and P. Nepa, "Reconfigurable modular antenna for NF UHF RFID smart point readers," *IEEE Trans. Antennas Propag.*, vol. 65, no. 2, pp. 498–506, Feb. 2017, doi: 10.1109/TAP.2016.2640140.

[18] M. A. S. Tajin and K. R. Dandekar, "Pattern reconfigurable UHF RFID reader antenna array," *IEEE Access*, vol. 8, pp. 187365–187372, 2020, doi: 10.1109/ACCESS.2020.3031296.

[19] K.-K. Duan and S.-Y. Cao, "Emerging RFID technology in structural engineering—A review," *Structures*, vol. 28, pp. 2404–2414, Dec. 2020, doi: 10.1016/j.istruc.2020.10.036.

[20] W. M. Abdulkawi and A. A. Sheta, "K-state resonators for high-coding-capacity chipless RFID applications," *IEEE Access*, vol. 7, pp. 185868–185878, 2019, doi: 10.1109/ACCESS.2019.2961565.

[21] Y. J. Zhang, R. X. Gao, Y. He, and M. S. Tong, "Effective design of microstrip-line chipless RFID tags based on filter theory," *IEEE Trans. Antennas Propag.*, vol. 67, no. 3, pp. 1428–1436, Mar. 2019, doi: 10.1109/TAP.2018.2879854.

[22] R. Bei et al., "Intrinsic low dielectric constant polyimides: Relationship between molecular structure and dielectric properties," *J. Mater. Chem. C*, vol. 5, no. 48, pp. 12807–12815, 2017, doi: 10.1039/C7TC04220E.

[23] Z. Yi, S. Xue, L. Xie, and G. Wan, "Detection of setting time in cement hydration using patch antenna sensor," *Struct. Control Health Monitor.*, vol. 29, no. 1, Jan. 2022, Art. no. e2855, doi: 10.1002/stc.2855.

Guochun Wan (Member, IEEE) received the Ph.D. degree in transportation information engineering and control from Tongji University, Shanghai, China, in 2011.

In 2006, he became an Associate Professor with the Department of Electronic Science and Technology, Tongji University. His current research interests focus on sensitive electronics, RFID sensors, circuit theory, and digital system design.

Zicheng Jiang received the B.S. degree in materials science and engineering from Tongji University, Shanghai, China, in 2021, where he is currently pursuing the master's degree in microelectronics science and engineering.

His current research interests include multiparameter sensor design, reconfigurable sensor design, and wireless detection methods for sensors.

Liyu Xie received the B.S. and M.S. degrees in mechanical engineering from Tongji University, Shanghai, China, in 2000 and 2003, respectively, and the Ph.D. degree in system design engineering from Keio University, Tokyo, Japan, in 2009.

In 2019, he became an Associate Professor with the College of Civil Engineering, Tongji University. His current research focuses on smart sensors, structural health monitoring (SHM), and structural vibration control.